RSC Advances

PAPER

View Article Online
View Journal | View Issue

Cite this: *RSC Adv.*, 2019, **9**, 7811

Supercapacitive performance of TiO_2 boosted by a unique porous TiO_2/Ti network and activated Ti^{3+}†

Qi Wang, Musen Li and Zhou Wang*

Received 31st December 2018
Accepted 4th March 2019

DOI: 10.1039/c8ra10671a

rsc.li/rsc-advances

TiO_2 has been reported to have considerable capacity through appropriate surface modification. Previous studies of TiO_2-based supercapacitors mainly focused on anodized TiO_2 nanotubes and TiO_2 powder, even though the capacitance still lags behind that of carbon-base materials. In this work, a three-dimensional porous TiO_2/Ti (PTT) network was constructed by anodic oxidation and its capacitance was boosted by subsequent aluminum-reduction process. Activated Ti^{3+} was proved to be being successfully introduced into the surface of pristine PTT, resulting in the prominent enhancement of supercapacitive performance. An areal capacitance of 81.75 mF cm^{-2} was achieved from Al-reduced PTT (Al-PTT) at 500 °C in 1 M H_2SO_4 electrolyte, which was among the highest value of pure TiO_2-based electrodes. Good electrochemical stability was also confirmed by the 3.12% loss of the highest capacity after 5000 CV cycles. More importantly, the activated Ti^{3+}/Ti^{4+} redox couple in modified TiO_2 is solidly confirmed by being directly observed in CV curves. The capacitive mechanism of the redox reaction is also studied by electrochemical tests. The construction of a 3D porous network structure and efficient Ti^{3+} introduction provide an effective method to boost the supercapacitive performance of TiO_2-based materials for energy storage applications.

Introduction

The popularity of mobile digital devices and the intensive development of electric vehicles are demanding increasingly superior removable electric power storage.[1] As a novel type of energy storage device, supercapacitors (also called ultracapacitors or electrochemical capacitors), combine the advantages of traditional capacitors and storage batteries, possessing the capacity to provide higher energy density than traditional capacitors and higher power density and longer cycle life than storage batteries.[2–4] In order to obtain higher-performance supercapacitors, various materials with different modifications have been adopted into to supercapacitors.[5–10] To obtain high specific capacitance, a favorable electrolyte is also a noteworthy point besides the intrinsic features and microstructure of the electrode material.

The electrodes of RuO_2 and carbon-based materials benefit much from acidic electrolytes, due to the enhanced electric double layer capacitance and pseudocapacitance by the massive adsorption and incorporation of protons.[11–13] Unfortunately, the conventional 3d-block pseudocapacitive metal oxides, such as MnO_2, NiO, Co_3O_4 and so forth, are unstable in acidic electrolytes, so that they cannot take this benefit. Luckily, TiO_2 is very stable in acid and it is an excellent oxide for proton absorption and incorporation, meaning a very promising pseudocapacitive material in acidic electrolytes. TiO_2-based materials have been constantly investigated to act as electrodes in supercapacitors, but TiO_2 holds a very low non-faradaic capacitance and almost no faradaic capacitance.[14–16] Because of poor electrochemical activity and weak electrical conductivity,[17,18] pristine TiO_2 electrode could hardly yield desirable specific capacitances.

Generally, the properties of nanoscale metal oxides including TiO_2 are usually very sensitive to oxygen content in the crystal lattice. The controlled introduction of Ti^{3+} and oxygen vacancies has been proved an effective way to increase the electrochemical activity and electrical conductivity of TiO_2.[19–21] Different methods have been tried to introduce oxygen vacancies to TiO_2, such as annealing in argon atmosphere,[16,22] facile cathodic reduction process,[20] and calcination in hydrogen atmosphere.[19] Due to the capability of providing high specific surface area and fast electron transfer path, TiO_2 nanotubes (TNT) fabricated by anodic oxidation has been chosen as research object.[19–21] The areal capacitances of modified TNT have been improved significantly, but still stay in a quite low level. Most areal capacitances of TNT earlier reported are below 20 mF cm^{-2}.[12,16,19–23] In a very recent work, reduced TNT was reported to achieve a high areal capacitance of 168 mF cm^{-2} at a current density of 1 mA cm^{-2}, which was claimed to be attributed to the Ti^{3+}/Ti^{4+} redox couple.[24] However, no redox peaks can be identified in CV curves, meaning unconfirmed activity of redox couple. On the other hand, the anodized TiO_2 nanotube layer with long tube length shrink, split and even

---

Key Laboratory for Liquid-Solid Structural Evolution and Processing of Materials, Ministry of Education, School of Materials Science and Engineering, Shandong University, Jinan, Shandong 250061, People's Republic of China. E-mail: wangzhou@sdu.edu.cn

† Electronic supplementary information (ESI) available. See DOI: 10.1039/c8ra10671a

exfoliate very easily during heat treatment caused by thermal stress, especially in hydrogen and other reductive gases. Therefore, the seeking for a better structure and a more powerful modification method for TiO_2 is still a critical issue.

Very recently, aluminum-reduction technique was developed and employed to reduce TiO_2 for enhanced photocatalytic property.[25,26] Inspired by a series of positive results, we propose Al-reduction as an alternative way to modify TiO_2 by introducing a certain amount of Ti^{3+} and oxygen vacancies to improve their capacitances. In this work, a unique 3D porous TiO_2/Ti (PTT) network structure was constructed and applied as active material to replace commonly used TNT. An areal capacitance of 81.75 mF cm^{-2} was achieved from Al-reduced PTT (Al-PTT) at 500 °C in 1 M H_2SO_4 electrolyte, which was among the highest value of pure TiO_2-based electrodes. Excellent electrochemical stability was also obtained by the 3.12% loss of highest capacity after 5000 CV cycles. Most interestingly, a pair of redox peaks can be clearly detected and located in CV curves, which provides a solid evidence of activated Ti^{3+}/Ti^{4+} redox couple. The capacitive mechanism of redox reaction was also discussed and confirmed based on electrochemical data.

Results and discussion

As shown in FE-SEM micrographs, raw Ti plate (Fig. 1a) shows relatively smooth surface with few shallow scratches. Titanium plate oxidized by simply immersed in H_2O_2 (denoted as Ti–H_2O_2) was set as the control group and its microstructure is shown in Fig. S1.† H_2O_2 etched and oxidized Ti plate simultaneously, resulting in a rough surface made up of nanoparticles with a diameter ~10 nm. In this work, anodizing voltage was considered as the key variable that affect the microstructure of PTT and was studied in detail.

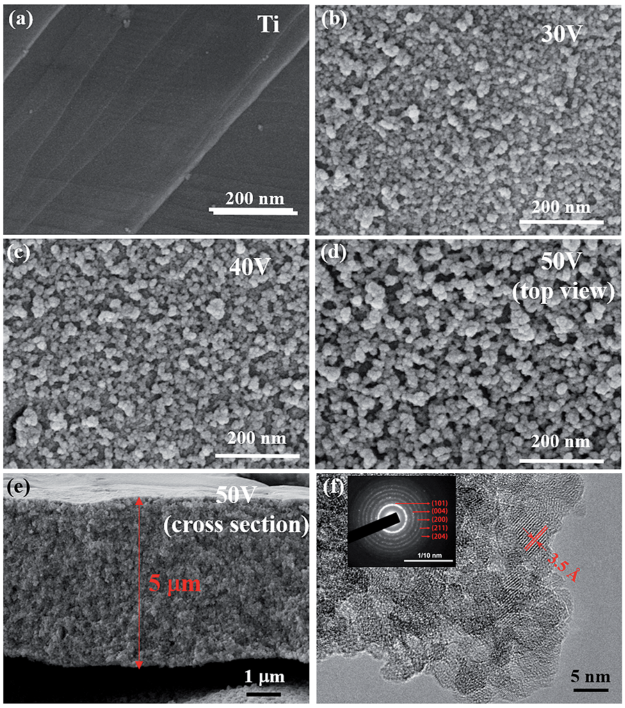

Fig. 1 Typical FE-SEM images: (a) raw Ti plate and Ti plate anodized at (b) 30 V, (c) 40 V, (d and e) 50 V. (f) HR-TEM images of Ti plate anodized at 50 V. The inset is the corresponding SAED pattern.

As can be seen in Fig. 1b–d, all anodized Ti plates applying different voltage exhibit rough surface assembled by nanoparticles, but detailed view in morphology are significantly different. For Ti plate anodized at 30 V (PTT-30), nanoparticles agglomerated and formed a relatively dense surface (Fig. 1b). When increasing the voltage to 40 V (PTT-40), porous structure can be detected but some areas still kept dense (Fig. 1c). Further increase of voltage to 50 V (PTT-50) led to a totally porous structure with interconnected network (Fig. 1d). The cross-section view (Fig. 1e) reveals that the oxidized layer is 5 μm in thickness with uniformly 3D-interconnected porous structure, which can simultaneously offer large surface area, efficient electron transfer path, good structural stability and strong mechanical properties, providing us an ideal structure for self-supported electrode in supercapacitor. The HR-TEM test of PTT reduced at 500 °C was also conducted to collect the information concerning composition, phase and lattice. As shown in Fig. 1f, the lattice fringes can be clearly observed and shows a spacing of 3.5 Å, close to that of 3.52 Å for (101) plane given in the JCPDS no. 21-1272 of anatase TiO_2. The inset is the pattern of selected area electron diffraction (SAED), which indicates the polycrystalline nature of the sample. The diameter of the diffraction rings fit well with the interplanar distance of (101), (004), (200), (211) and (204) planes of anatase TiO_2 respectively, which confirms the formation of anatase TiO_2 during the anodization.

By applying proper method, the optimized structure of PTT has been obtained. But the fundamental problems of TiO_2 (low conductivity, high stability for Ti^{4+}) as active material for supercapacitor remain unsolved. Inspired by previous reports, the method of Al-reduction was conducted in order to improve the performance of our PTT. Different reduction temperatures (350 °C, 500 °C, 650 °C) were studied comparatively and the microstructures are shown in Fig. 2a–c. PTT reduced at 350 °C show no obvious difference with primary PTT. After reduced at 500 °C, the 3D porous structure remained the same, except for the mild growth and fusion of crystalline grains, resulting in larger particles and thicker "wires" of the network. Higher reduction temperature at 650 °C led to severe recrystallization,

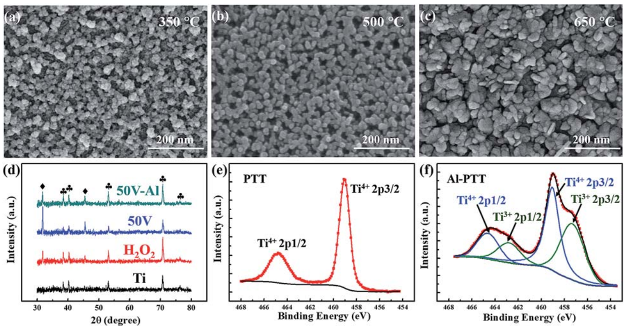

Fig. 2 Typical FE-SEM images of PTT-50 reduced at (a) 350 °C, (b) 500 °C, (c) 650 °C. (d) X-ray diffraction patterns of Ti plates before and after different treatment (◆: anatase TiO_2, ♣: Ti). Ti 2p XPS spectra of (e) PTT-50 and (f) Al-PTT-50.

which blocked the channels of network and completely destroyed the porous structure.

The EDS elemental mapping of PTT and PTT reduced at 500 °C are shown in Fig. S2 and S3.† O element and Ti element shows uniform distribution on the surface of the plate for both samples but the content of oxygen decreased from 26% to 22.5% after reduction, indicating effective extraction of oxygen by aluminum reduction.

The BET measurement of PTT reduced at 500 °C was conducted (Fig. S4†), which shows a Type IV isotherm characteristic of mesoporous materials, featuring an H2 hysteresis loop. The specific surface area was 9.19 $m^2\ g^{-1}$ with an average BJH pore diameter of ∼20 nm. However, it should be noted that this result is much lower than the real value because the porous TiO_2 layer was attached firmly on the Ti metal substrate, and hence, the exact weight of the porous TiO_2 layer can't be determined.[27]

Fig. 2d presents the XRD patterns of PTT treated with different process. The curve of raw Ti exhibits diffraction peaks at 38.5°, 40.2°, 53.1°, 70.7°, 76.2°, which can all be indexed in accordance with standard card of pure titanium (JCPDS no. 44-1294). No other peaks were found in the pattern of Ti plate, verifying the purity of Ti plate and the negligible surface oxide layer. After treated with H_2O_2 or anodized at 50 V, the previously mentioned peaks of Ti remains and two new peaks at 31.8° and 45.5° appeared, which coincides with the (101) and (200) plane of anatase TiO_2 (JCPDS no. 21-1272). It must be noted that, the intensity of peaks related to anatase TiO_2 obviously increased for anodized sample. Herein, we proposed a simple method to evaluate the relative content by simply compare the intensity ratio of peaks at 31.8° and 70.7° (denoted as I_{TiO_2}/I_{Ti}). As can be seen in Fig. 2d, anodizing process induced a significant increase of peak intensity at 31.8° and simultaneously cut the peak intensity at 70.7°, which means plenty of TiO_2 formed on the surface of Ti plates. Heat treatment is generally considered to increase the crystallinity of materials, but reduction at 500 °C led to a decreased value of I_{TiO_2}/I_{Ti}, which can be ascribed to the severe lattice disorder induced by the loss of lattice oxygen.

Fig. 2e and f shows the Ti 2p XPS spectra of PTT and Al-PTT. Ti^{4+}–O bonds can be obviously verified by the two peaks centered at the binding energies of 459.1 eV and 464.8 eV, which correspond to the characteristic peaks of Ti $2p_{3/2}$ and Ti $2p_{1/2}$ in Ti^{4+}–O bonding structure.[28,29] Compared with pristine PTT, the additional small peaks located respectively at 457.4 eV and 462.9 eV in Al-PTT conform to the $2p_{3/2}$ and $2p_{1/2}$ peaks of Ti^{3+},[29,30] which is attributed to the considerable intake of Ti^{3+} states in the surface of Al-PTT *via* the Al-reduction process.

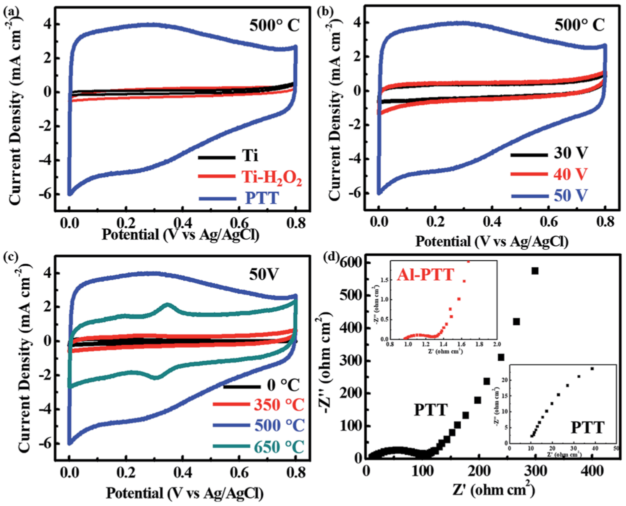

Fig. 3 CV curves of electrodes reduced at 500 °C at the scan rate of 50 mV s^{-1}: (a) raw Ti, Ti–H_2O_2, PTT-50; (b) raw Ti, PTT-30, PTT-40, PTT-50. (c) PTT-50 reduced at different temperatures ranging from 0 to 650 °C. (d) Nyquist plots of PTT-50 and Al-PTT-50, insets are enlargements of the high frequency regions.

Fig. 3a shows the CV curves of raw Ti plate, Ti–H_2O_2 and PTT-50 (all reduced at 500 °C) recorded at a scan rate of 50 mV s^{-1}. Raw Ti plate shows a low current density of ∼0.1 mA cm^{-2} at 0.4 V, which can be ascribed to its metallic properties and low surface area. The current density increased slightly for Ti–H_2O_2 electrode, which mainly originated from the increase of surface area. The previous SEM image reveals that the etching and oxidizing effect of H_2O_2 only conducted on the shallow surface of Ti plate, which can explain the weak increase of current density. The rechargeable current density of reduced PTT-50 increases dramatically and displays an approximately rectangular shaped CV curve as expected from an ideal capacitor, demonstrating a significant increase in supercapacitive performance. As mentioned before, different voltages were applied in the anodizing process and the CV curves of the corresponding reduced samples were recorded (Fig. 3b). The reduced PTT-30 and PTT-40 electrodes show similar supercapacitive performance with a current density of ∼0.5 mA cm^{-2} at 0.4 V, which is almost one eighth of the current density of reduced PTT-50. The undeveloped performance of PTT-30 and PTT-40 is mainly due to their insufficient anodizing, resulting in thin oxidation layer and the absence of 3D porous structure. Through the previous comparison, the PTT-50 is believed to have the optimized microstructure which facilitates the energy storage process.

Based on the unique porous structure, our focus switched to improving its electrochemical property. Different temperatures were applied during the reduction process and the CV curves are shown in Fig. 3c. Before reduction, the shape of the CV curve is triangular, revealing the high resistance caused by the nonconductive oxide layer. After reduced at 350 °C, the current density only gains a slight increase but the shape of curve turns close to rectangle, demonstrating the improvement of relatively lower resistance. Reduction at 500 °C brought a dramatic increase in capacitive current density and corresponding areal capacitance, which can be ascribed to the reduced resistivity and activated Ti^{3+}/Ti^{4+} redox couple. Two obscure redox peaks at ∼0.29 V/∼0.23 V can be identified in the CV curve. There is an approximate Arrhenius relationship between the content of Ti^{3+} and the temperature described in previous literature:[24]

$$n = n_0 \exp(-\Delta E/kT),$$

where n is the molar content of Ti^{3+}, n_0 is a fitting coefficient, ΔE is the escape energy of O atoms from TiO_2 in Al-reduction, and T is the temperature. Therefore, carrier density continuously rises when increasing Al-reduction temperature. However, further increased reduction temperature at 650 °C led to an attenuated current density and areal capacitance, which can be attributed to the degeneration of porous structure (Fig. 2c) induced by recrystallization. Interestingly, a pair of cathodic/anodic peaks centred at 0.35 V/0.30 V was clearly observed and located for the first time in pure TiO_2-based supercapacitor. Based on the truth that the electrode only contains two elements (titanium and oxygen) according to XPS full spectrum analysis, the redox peaks can be certified as cathodic/anodic peaks of Ti^{3+}/Ti^{4+} redox reaction. The emergence of the sharp redox peaks can be attributed to two reasons: (1) higher reduction temperature can produce higher concentration of Ti^{3+} and severe lattice disorder, thus providing more activated Ti^{3+}/Ti^{4+} redox couple, which enhanced the intensity of Ti^{3+}/Ti^{4+} redox peaks in CV curve. (2) The collapse of porous structure for PTT reduced at 650 °C resulted in a sharp decrease of surface area, dramatically cut the portion of double-layer capacitance and led to the more conspicuous redox peaks.

Typical Nyquist plots with frequencies ranging from 0.01 to 100 kHz are shown in Fig. 3d. PTT-50 reduced at 500 °C exhibits a much lower impedance value than pristine PTT, further demonstrating the great improvement of electrical conductivity. The intercept of the curve in the high-frequency region on the real axis is assigned to the ohmic series resistance (R_s). The significantly smaller R_s (0.96 Ω cm^2) of Al-PTT than that (10.45 Ω cm^2) of pristine PTT also proves the enhanced electrical conductivity induced by Al-reduction. The semicircle in the high-frequency range is related to the charge-transfer resistance (R_{ct}) between the electrode and electrolyte, which can be evaluated by the semicircle diameter. Al-PTT electrode possesses a distinctly smaller semicircle diameter than that of pristine PTT electrode, validating its lower R_{ct} as a result of the improved electrochemical activity.

CV curves of Al-PTT-50 electrode collected under different scan rates from 2 to 200 mV s^{-1} are shown in Fig. 4a. The rectangular consistency of these curves at various scan rates reveals excellent capacitive behaviour. Fig. 4b depicts the GCD curves of Al-PTT-50 at different current densities. At higher current densities, the voltage is almost linearly related to the charge–discharge time. With the decrease of current density, little nonlinearity of the curves can be detected, which typically indicates faradaic reactions happens during the charge–discharge process.[21] We propose that the capacitance of Al-PTT is a hybrid contribution of the minor electrical double-layer capacitance and the dominant faradaic pseudocapacitance, according to the GCD curves. The pseudocapacitance mainly derives from the oxidation–reduction reaction based on the valence transition of Ti^{3+}/Ti^{4+} due to the existence of considerable Ti^{3+} in Al-PTT. Therefore, the Al-reduction treatment contributes much to the enhanced pseudocapacitance of PTT, as well as the electrical double-layer capacitance.

Fig. 4c presents the areal capacitances of origin PTT-50 and Al-PTT-50 electrodes calculated from CV curves, which exhibit a huge gap in the areal capacitance level. At the scan rate of 2 mV s^{-1}, the areal capacitance of Al-PTT-50 is 81.75 mF cm^{-2}, which is 134 times higher than that of PTT (0.61 mF cm^{-2}). Although the performance of our PTT electrode still lags behind Ni/Co/Mn oxide based electrodes due to the limitation of TiO_2,[31–33] our work made a huge progress on boosting supercapacitive performance of TiO_2 and obtained far superior capacitance (81.75 mF cm^{-2}) than that of pure TiO_2-based materials reported in previous studies, such as pristine TiO_2 (2.4 mF cm^{-2}), H_2 annealed TiO_2 (3.24 mF cm^{-2}), nitrided TiO_2 (3.14 mF cm^{-2}), plasma treated TiO_2 (7.22 mF cm^{-2}), electrochemical reduced TiO_2 (20.08 mF cm^{-2}), hydrogenated TiO_2 (24 mF cm^{-2}), and black TiO_2 (15.6 mF cm^{-2}).[12,16,19–23] Such excellent performance can be attributed to two major reasons. First, PTT can be reduced easily and deeply at the sustaining low oxygen partial pressure created by melting aluminium during the Al-reduction process.[25] Second, PTT with the unique 3D porous network structure possesses higher surface area, faster electron transfer channel and stronger mechanical property than other nanostructure built on Ti substrate in previous literature. Commonly used anodized TiO_2 nanotube layer with greater tube length shrink, split and even exfoliate very easily during heat treatment caused by thermal stress, especially in hydrogen and other reductive gases. Nevertheless, similar case does not happen to our Al-PTT, because of the good mechanical property and gent and uniform reduction process. When the scan rate increases from 2 to 200 mV s^{-1}, an areal capacitance of

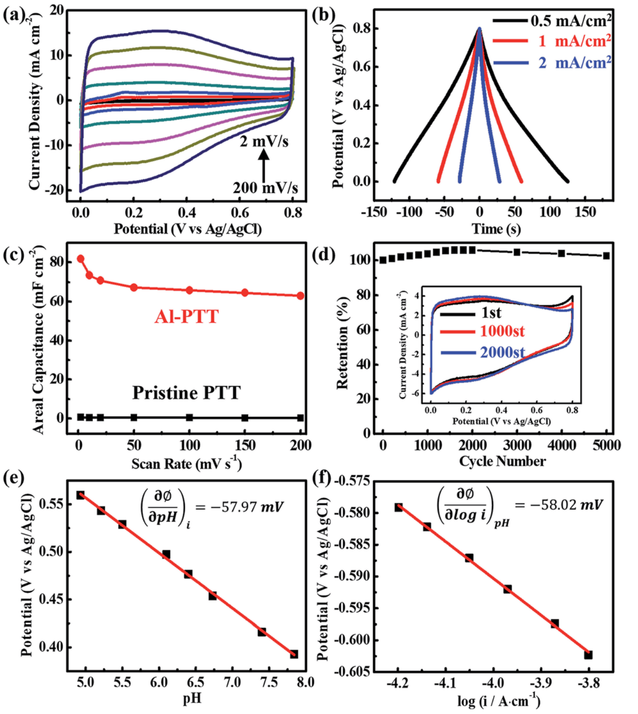

Fig. 4 (a) CV curves of Al-PTT-50 electrode collected under different scan rates ranging from 2 to 200 mV s^{-1}. (b) GCD curves of Al-PTT-50 electrode collected at different current densities ranging from 0.5 to 2 mA cm^{-2}. (c) Areal capacitances of origin PTT and Al-PTT-50 electrodes calculated from CV curves under different scan rates. (d) Retention of initial areal capacitance of Al-PTT-50 electrode, calculated from CV curves (at the scan rate of 50 mV s^{-1}) of different cycles, and CV curves of the 1st, 1000th, 2000th cycle are present in the inset. (e) pH dependence of steady-state potential for Al-PTT-50 at 0.5 μA cm^{-2} in 1 M KH_2PO_4 solution. (f) Electrode potential as a function of current density in the Tafel zone characterized in 1 M H_2SO_4.

63.0 mF cm^{-2} remains with a capacity retention of 77.0%, which reveals good rate capability of our Al-PTT. In contrast, the retention of origin PTT is merely 24.6% at the same condition.

In order to examine the cycling stability of Al-PTT, CV measurement was conducted for successive 5000 cycles at the scan rate of 50 mV s^{-1}. The calculated areal capacitances from CV curves are present in Fig. 4d, as well as the CV curves of the first, 2000th and 3000th cycles. Interestingly, the capacity increases gradually in the first 1600 cycles and finally gains more than 5.82% increase at the 1600th cycle. The capacity keeps steady during 1600th to 2000th cycles and decays very slowly afterward, obtaining 96.88% retention of the highest capacity (at 2000th cycle) after 5000 cycles. As can be seen in the inset image of Fig. 4d, the raise of CV curves at high potential turns flat, while the intensity of redox peaks increases gradually. The raise near the edge of potential window is commonly believed to be ascribed to the polarization of electrode. The vanish of the raise tail is probably cause by the improving infiltration of electrolyte in the porous structure. Although the increasing peak intensity of redox couple and the improved capacitance can also be explained by the better infiltration, we would like to propose another possible reason that the charge/discharge process may activate the Ti^{3+}/Ti^{4+} redox reaction.

The two electrode system was assembled by using reduced graphene oxide (rGO) as negative electrode and 1 M H_2SO_4 as electrolyte. The CV curves obtained under different scan rates (Fig. S5a†) show rectangle shape and the stable potential window of the device can be extended to 1.2 V without obvious polarization peak. Fig. S5b† shows the GCD curves of the device at different current density, and the calculated specific capacitance is 15.18 mF cm^{-2} at a current density of 0.5 mA cm^{-2}. The energy density and power density of ASC device can be calculated by the following equation:

$$E = 1/2CV^2$$

$$P = E/t$$

where '*C*' is the specific capacity, '*V*' is the working potential window, '*t*' is the discharge time. The energy density is calculated by GCD curves and shows the maximum value of 10.9 mW h cm^{-2} at a power density of 300 mW cm^{-2}.

In order to explore the capacitive mechanism of reduced PTT, we performed the pH dependent steady-state potential test and Tafel tests to probe the reaction thermodynamics. Based on the very low ESR of reduced PTT, the measured voltage is assumed close to the actual reaction potential for the electrode, which has a linear relationship with pH (Fig. 4e) and the steady-state current (Fig. 4f). Therefore, we propose the following redox reactions that the pseudocapacitance of reduced PTT origins from the intercalation/chemisorption of the proton on the solid surface, as shown below:

$$TiO_{2-x} + yH^+ + ye \leftrightarrow TiO_{2-x-y}(OH)_y,$$

where TiO_{2-x} represents the product of Al-reduction. During the redox reaction, the electrochemical driving force ΔG for an intercalation/chemisorption reaction that involves z electrons can be represented as $\Delta G = -zF\phi + RT\ln(\alpha(H^+))$, where ϕ is the electrode potential and $\alpha(H^+)$ is proton activity. So $\exp(-\Delta G/RT)$ and the steady-state reaction current I can follow the equation below:

$$I = i_0\alpha(H^+)^{-1}\exp\left(\frac{zF\phi}{RT}\right)$$

where F means the Faraday constant, i_0 represents for a proportionality constant, R is the molar gas constant, and T is temperature.[14] The data in Fig. 2e and f shows that the slopes in the curves, $\partial\phi/\partial\log[H^+]$ and $\partial\phi/\partial\log(i)$, are −57.97 mV per decade and −58.02 mV per decade, respectively, consistent with the value of 59.2 mV per decade that corresponds to $2.3 \times RT/F$. Based on the value of slope for two curves, we can determined that $z = 1$ for reduced PTT, which means each active site receives one electron and one proton during the redox reaction.

Experimental

Preparation of PTT and Al-PTT

The synthetic route our sample is illustrated in Fig. S6.† The PTT were prepared on Ti plate (99.5% purity, 20 μm in thickness, Alfa Aesar) *via* one-step electrochemical anodization process with Pt plate as the cathode. The electrolyte was consisted of 10 wt% K_2HPO_4 dissolved in anhydrous glycol. The Ti plate was anodized at different voltage (30 V, 40 V, 50 V) supplied by an Auto Range DC Power Supply (ITECH IT6720, China) for 10 hours. After slowly cooling, cleaning with water and drying in air, the as-prepared PTT were annealed at 500 °C for 8 hours in an Al-reduction device (denoted as Al-PTT). When conducting Al-reduction process, PTT samples and aluminum powder were placed separately in a two-zone tube furnace and then evacuated to a base pressure below 5 Pa. Subsequently, PTT samples and aluminum powder were heated to 500 °C and 800 °C respectively, and kept for 8 hours. The details about Al-reduction device and mechanism were clearly described in our previous report.[25]

Characterization

To investigate the microstructure and composition of the samples, field emission scanning electron microscope (FE-SEM, JEOL JSM-6700F), high resolution transmission electron microscope (HR-TEM, JEOL JEM-2011), specific surface and aperture analyzer (Builder Kubo-X1000), X-ray diffraction (XRD, Bruker AXS D8 Advance), X-ray photoelectron spectroscopy (XPS, ThermoFisher SCIENTIFIC ESCALAB 250) were employed.

Electrochemical measurements

To characterize the electrochemical performance of the samples, a conventional three-electrode system was utilized to conduct electrochemical measurements. The PTT assembled on Ti substrates were used directly as the working electrode, with a Pt plate and an Ag/AgCl (KCl saturated) electrode as counter and reference electrodes respectively in 1 M H_2SO_4 aqueous solution. Electrochemical impedance spectroscopy (EIS), cyclic voltammetry (CV) and galvanostatic charge–discharge (GCD) tests were carried out by an electrochemical workstation (IviumStat Vertex. 1A. EIS). Nyquist plots were acquired from AC impedance tests performed over a frequency range of 0.01 Hz to 100 kHz at an amplitude of 5 mV. The cycling stability was tested by CV measurements at a constant scan rate of 50 mV s^{-1} for 5000 cycles.

Conclusions

In conclusion, Al-reduction has been demonstrated to be an effective method to introduce Ti^{3+} and lattice disorder into our unique 3D porous TiO_2/Ti network, so as to improve its electrochemical activity and electrical conductivity dramatically. The Al-PTT electrode is capable of producing an areal capacitance of 81.75 mF cm^{-2}, which is among the highest value for TiO_2-based electrodes. Good electrochemical stability has also been confirmed by the 3.12% loss ratio after 5000 CV cycles. The activated redox couple of Ti^{3+}/Ti^{4+} is clearly detected in pure TiO_2-based materials by CV for the first time and the capacitive mechanism is proposed based on solid electrochemical data. The Al-PTT are promising to be used as candidates for applications in other energy-related areas such as solar cell, lithium battery.

Conflicts of interest

There are no conflicts to declare.

Acknowledgements

This work was supported by the National Natural Science Foundation of China (No. 51502159, No. 51702188), the Natural Science Foundation for Outstanding Young and Middle-aged Scientists of Shandong Province (Grant No. BS2015CL001), the Young Scholars Program of Shandong University (2018WLJH25), and the Fundamental Research Funds of Shandong University (2014HW019, 2017TB0024).

References

1 G. P. Wang, L. Zhang and J. J. Zhang, A review of electrode materials for electrochemical supercapacitors, *Chem. Soc. Rev.*, 2012, **41**, 797–828.
2 B. E. Conway, Transition from supercapacitor to battery behavior in electrochemical energy-storage, *J. Electrochem. Soc.*, 1991, **138**, 1539–1548.
3 S. G. Kandalkar, D. S. Dhawaleb, C.-K. Kim and C. D. Lokhande, Chemical synthesis of cobalt oxide thin film electrode for supercapacitor application, *Synth. Met.*, 2010, **160**, 1299–1302.
4 C. Largeot, C. Portet, J. Chmiola, P.-L. Taberna, Y. Gogotsi and P. Simon, Relation between the ion size and pore size for an electric double-layer capacitor, *J. Am. Chem. Soc.*, 2008, **130**, 2730–2731.
5 D. N. Futaba, K. Hata, T. Yamada, T. Hiraoka, Y. Hayamizu, Y. Kakudate, O. Tanaike, H. Hatori, M. Yumura and S. Iijim, Shape-engineerable and highly densely packed single-walled carbon nanotubes and their application as super-capacitor electrodes, *Nat. Mater.*, 2006, **5**, 987–994.
6 J. Gamby, P. L. Taberna, P. Simon, J. F. Fauvarque and M. Chesneau, Studies and characterisations of various activated carbons used for carbon/carbon supercapacitors, *J. Power Sources*, 2001, **101**, 109–116.
7 J. W. Lang, L. B. Kong, W. J. Wu, Y. C. Luo and L. Kang, Facile approach to prepare loose-packed NiO nano-flakes materials for supercapacitors, *Chem. Commun.*, 2008, **35**, 4213–4215.
8 L. Z. Fan and J. Maier, High-performance polypyrrole electrode materials for redox supercapacitors, *Electrochem. Commun.*, 2006, **8**, 937–940.
9 A. Laforgue, P. Simon, C. Sarrazin and J. François, Polythiophene-based supercapacitors, *J. Power Sources*, 1999, **80**, 142–148.
10 K. S. Ryu, K. M. Kim, N. G. Park, Y. J. Park and S. H. Chang, Symmetric redox supercapacitor with conducting polyaniline electrodes, *J. Power Sources*, 2002, **103**, 305–309.
11 J. T. Zhang, J. Z. Ma, L. L. Zhang, P. Z. Guo, J. W. Jiang and X. S. Zhao, Template synthesis of tubular ruthenium oxides for supercapacitor applications, *J. Phys. Chem. C*, 2010, **114**, 13608–13613.
12 Y. Xie, Y. Wang and H. Du, Electrochemical capacitance performance of titanium nitride nanoarray, *Mater. Sci. Eng., B*, 2013, **178**, 1443–1451.
13 E. G. Calvo, F. Lufrano, P. Staiti, A. Brigandì, A. Arenillas and J. A. Menéndez, Optimizing the electrochemical performance of aqueous symmetric supercapacitors based on an activated carbon xerogel, *J. Power Sources*, 2013, **241**, 776–782.
14 B. Chen, J. B. Hou and K. Lu, Formation mechanism of porous TiO_2/Ti and their applications in photoelectrochemical water splitting and supercapacitors, *Langmuir*, 2013, **29**, 5911–5919.
15 T. Brezesinski, J. Wang, J. Polleux, B. Dunn and S. H. Tolbert, Templated nanocrystal-based porous TiO_2 films for next-generation electrochemical capacitors, *J. Am. Chem. Soc.*, 2009, **131**, 1802–1809.
16 M. Salari, S. H. Aboutalebi, K. Konstantinova and H. K. Liua, A highly ordered titania nanotube array as a supercapacitor electrode, *Phys. Chem. Chem. Phys.*, 2011, **13**, 5038–5041.
17 F. F. Santiago, E. M. Barea, J. Bisquert, G. K. Mor, K. Shankar and C. A. Grimes, High carrier density and capacitance in TiO_2 nanotube arrays induced by electrochemical doping, *J. Am. Chem. Soc.*, 2008, **130**, 11312–11316.
18 J. Wang, J. Polleux, J. Lim and B. Dunn, Pseudocapacitive contributions to electrochemical energy storage in TiO_2 (anatase) nanoparticles, *J. Phys. Chem. C*, 2007, **111**, 14925–14931.
19 X. H. Lu, G. M. Wang, T. Zhai, M. H. Yu, J. Y. Gan, Y. X. Tong and Y. Li, Hydrogenated TiO_2 nanotube arrays for supercapacitors, *Nano Lett.*, 2012, **12**, 1690–1696.
20 H. Zhou and Y. R. Zhang, Enhancing the capacitance of TiO_2 nanotube arrays by a facile cathodic reduction process, *J. Power Sources*, 2013, **239**, 128–131.
21 M. Salari, K. Konstantinov and H. K. Liu, Enhancement of the capacitance in porous TiO_2/Ti through controlled

introduction of oxygen vacancies, *J. Mater. Chem.*, 2011, **21**, 5128–5133.

22 M. Salari, S. H. Aboutalebi, A. T. Chidembo, I. P. Nevirkovets, K. Konstantinova and H. K. Liu, Enhancement of the electrochemical capacitance of TiO_2 nanotube arrays through controlled phase transformation of anatase to rutile, *Phys. Chem. Chem. Phys.*, 2012, **14**, 4770–4779.

23 Y. B. Xie and D. G. Fu, Photochemical performance and electrochemical capacitance of titania nanocomplexes, *Mater. Res. Bull.*, 2010, **45**, 628–635.

24 J. Zhi, H. L. Cui, Z. Wang and F. Q. Huang, Surface confined titania redox couple for ultrafast energy storage, *Mater. Horiz.*, 2018, **5**, 691–698.

25 Z. Wang, C. Y. Yang, T. Q. Lin, H. Yin, P. Chen, D. Y. Wan, F. F. Xu, F. Q. Huang, J. H. Lin, X. M. Xie and M. H. Jiang, Visible-light photocatalytic, solar thermal and photoelectrochemical properties of aluminium-reduced black titania, *Energy Environ. Sci.*, 2013, **6**, 3007–3014.

26 G. L. Zhu, T. Q. Lin, X. J. Lü, W. Zhao, C. Y. Yang, Z. Wang, H. Yin, Z. Q. Liu, F. Q. Huang and J. H. Lin, Black brookite titania with high solar absorption and excellent photocatalytic performance, *J. Mater. Chem. A*, 2013, **1**, 9650–9653.

27 D. R. Baker and P. V. Kamat, Disassembly, reassembly, and photoelectrochemistry of etched TiO_2 nanotubes, *J. Phys. Chem. C*, 2009, **113**, 17967–17972.

28 X. B. Chen, L. Liu, P. Y. Yu and S. S. Mao, Increasing solar absorption for photocatalysis with black hydrogenated titanium dioxide nanocrystals, *Science*, 2011, **331**, 746–750.

29 X. D. Jiang, Y. P. Zhang, J. Jiang, Y. S. Rong, Y. C. Wang, Y. C. Wu and C. X. Pan, Characterization of oxygen vacancy associates within hydrogenated TiO_2: a positron annihilation study, *J. Phys. Chem. C*, 2012, **116**, 22619–22624.

30 M. M. Rahman, K. M. Krishna, T. Soga, T. Jimbo and M. Umeno, Optical properties and X-ray photoelectron spectroscopic study of pure and Pb-doped TiO_2 thin films, *J. Phys. Chem. Solids*, 1999, **60**, 201–210.

31 A. K. Yedluri and H.-J. Kim, Enhanced electrochemical performance of nanoplate nickel cobaltite ($NiCo_2O_4$) supercapacitor applications, *RSC Adv.*, 2019, **9**, 1115–1122.

32 S. Y. Zhang, Y. C. Pang, Y. K. Wang, B. T. Dong, S. Y. Lu, M. Y. Li and S. J. Ding, NiO nanosheets anchored on honeycomb porous carbon derived from wheat husk for symmetric supercapacitor with high performance, *J. Alloys Compd.*, 2018, **735**, 1722–1729.

33 Y. C. Pang, S. Y. Zhang, S. Chen, J. Liang, M. Y. Li, D. W. Ding and S. J. Ding, Transition-metal oxides anchored on nitrogen-enriched carbon ribbons for high-performance pseudocapacitors, *Chem. –Eur. J.*, 2018, **24**, 16104–16112.